Editors' Suggestion | Featured in Physics

Femtosecond and Attosecond Phase-Space Correlations in Few-Particle Photoelectron Pulses

Rudolf Haindl, Valerio Di Giulio,* Armin Feist, and Claus Ropers†
Department of Ultrafast Dynamics, Max Planck Institute for Multidisciplinary Sciences, D-37077 Göttingen, Germany and 4th Physical Institute—Solids and Nanostructures, University of Göttingen, D-37077 Göttingen, Germany

(Received 31 December 2024; revised 2 June 2025; accepted 28 July 2025; published 15 October 2025)

Temporal correlations in pulsed electron beams reflect the microscopic dynamics of emission and interparticle interaction. In femtosecond electron emission from nanoscale field emitters, Coulomb interactions result in structured few-electron states with strong correlations in energy, time, and transverse momentum. Interactions with external fields may be used to both probe and further manipulate these correlated states. Here, we combine femtosecond-gated, event-based detection with inelastic electron-light scattering to directly map the photoelectron phase-space distribution of two-electron states. Our experiments demonstrate a bimodal structure in longitudinal phase space, with distinct contributions from interparticle interaction and dispersion. Moreover, we imprint a global phase modulation onto two-electron states and theoretically show that coherent shaping of few-electron phase-space distributions enables attosecond temporal correlations. This controlled phasing of few-electron states can be harnessed to produce tailored excitations and superradiance via two-electron energy postselection.

DOI: 10.1103/lylq-m63c

The Coulomb interaction among electrons forming a beam remains a longstanding challenge for electron microscopy and spectroscopy. Limiting contrast and resolution, longitudinal [1] and transverse [2] scattering manifests as anticorrelations in the time of arrival [3] as well as the transverse position and momentum [4–8] at the detector plane. In pulsed electron beams produced by photoemission from nanotip field emitters [9–11], event-based detection recently uncovered pronounced Coulomb-induced energy correlations in an electron microscope [8] and at free-standing nanotips [12]. The understanding of such correlations promotes novel measurement schemes based on controlled few-electron states, underlying recent proposals of shot noise-reduced imaging [8,13] and multiparticle sample excitations [14–24], where excitation enhancement is achieved either via pulse compression or periodic bunching. Moreover, multielectron states are expected to enhance dose-sensitive imaging [25,26] and quantum-mechanical electron-light entanglement [27–33].

The phase-space distribution of pulsed electron beams is particularly relevant in the context of ultrafast electron microscopy, combining high temporal and spatial resolutions [34–41]. On the one hand, typically low duty cycles in ultrafast imaging, diffraction, and spectroscopy aim for maximum allowable pulse charge, which renders Coulomb interactions an essential constraint in this technology. On the other hand, ultrafast microscopes offer ideal conditions to study the correlations among few-electron ensembles within a well-defined temporal gate. Several effects govern the spectral and temporal distribution of electron pulses, which involve the photoemission process [9–11,42–46] as well as Coulomb interactions [8,36,47–49]. Measurements of the time structure of electron pulses can be obtained by electron-laser cross-correlation using ponderomotive scattering [50] or streaking [51,52], recently performed for few-electron states [40]. Femtosecond-resolved temporal slicing [35,36,53,54] based on inelastic electron-light interaction [55–57] has shown a broadening of the phase-space distribution with increasing average current. However, mean-field and stochastic interactions are expected to affect pulse dispersion in distinct ways, which calls for the measurement and active shaping of electron-number specific phase-space distributions for tailored probing.

In this Letter, we present the measurement and control of two-electron states using inelastic electron-light scattering (IELS). Employing femtosecond temporal gating in an ultrafast transmission electron microscope (UTEM), we record time-energy correlation maps of Coulomb-correlated two-electron pulses and reconstruct their joint phase-space distributions. To support these observations, we formulate IELS in the multielectron regime and perform numerical simulations that reproduce the measured energy-time

*Contact author: valerio.digiulio@mpinat.mpg.de
†Contact author: claus.ropers@mpinat.mpg.de

Published by the American Physical Society under the terms of the Creative Commons Attribution 4.0 International license. Further distribution of this work must maintain attribution to the author(s) and the published article's title, journal citation, and DOI. Open access publication funded by the Max Planck Society.

correlations at the sample plane. Finally, we demonstrate that coherent IELS enables the preparation of attosecond-scale interparticle correlations, allowing for active control and enhancement of nanoscale excitations, without requiring dispersive bunching of the electron ensemble.

Optimized electron pulse properties are of central importance in ultrafast electron microscopy. The longitudinal properties of multielectron ensembles are fully described by the $2n$-dimensional phase-space density $\rho_n(\{t_i\},\{E_i\})$, where $\{t_i\}$ and $\{E_i\}$ denote the set of n time and energy variables. Given the high dimensionality of $\rho_n(\{t_i\},\{E_i\})$, marginal phase-space densities are often sufficient to analyze beam properties and determine the achievable energy and time resolution. These may be expressed in terms of the overall densities $\rho(t,E)$, or number-sorted as $\rho_n(t,E)$.

This Letter aims to characterize and optically shape the number-resolved phase-space properties of few-electron pulses in a field-emitter UTEM [Fig. 1(a)]. To illustrate Coulomb- and propagation-induced correlations, we analyze two-electron trajectory simulations predicting the evolution of $\rho_2(t,E)$ at various positions in the microscope (see End Matter). Initially, the electron pair is emitted with normally distributed time and energy [Fig. 1(b), panel i], assuming no nascent correlations. Subsequently, the electrons are electrostatically accelerated along the beam direction. To a good approximation, the momentary rate of Coulomb-induced energy exchange is given by the Coulomb force times the mean velocity of the two electrons, which leads to an increasing difference in kinetic energy (panel ii). As the accelerating field weakens, the kinetic energy difference saturates, and dispersion translates energy into temporal correlations (panels iii and iv).

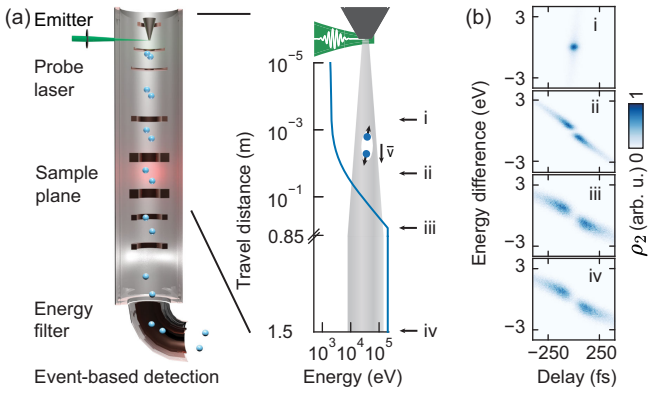


FIG. 1. Generation and propagation of two-electron pulses in a field-emitter ultrafast transmission electron microscope. (a) Schematic showing increasing temporal separation of a Coulomb-correlated photoelectron pair (left) accelerated to 200 keV (right) and recorded with an event-based detector behind an electron spectrometer. Note the logarithmic position scale during acceleration. (b) Simulated evolution of the longitudinal phase-space distribution for different locations along the column (i–iv), illustrating the concurrent buildup of energy correlations and dispersive pulse broadening.

In the transmission electron microscope (JEM F200, JEOL) [see Fig. 1(a)], we generate few-particle electron pulses by close-to-threshold photoemission from a Schottky emitter [8,35,36,43] with a femtosecond laser. The number of electrons emitted by each laser pulse follows moderately antibunched statistics [8], with a power-dependent emission rate of n-electron events per laser pulse r_n and a transmission into the column of below 5%. Electron pulses are accelerated to 7 keV in an emitter assembly with extraction and focusing electrodes and subsequently to a beam energy of $E_0 = 200$ keV. Spectral analysis is performed with an energy filter and a nanosecond-resolution event-based camera (Timepix3 ASIC) [58]. Our detection scheme [8,59] correlates the electrons with the generating laser pulses, enabling electron-number classification.

The ensemble phase-space densities are reconstructed by ultrafast gating of the electron pulses. Conceptually, we relate $\rho_n(\{t_i\},\{E_i\})$ to measurable electron energy spectra by exploiting IELS, a process where electrons are efficiently coupled to optical near fields [35,36,53,57]. Here, few-electron states arriving in coincidence with an out-of-plane-polarized optical near field in the sample plane at time t_L are inelastically scattered by multiples of the photon energy. In this regard, the recorded spectral maps $\langle\Gamma(t_\mathrm{L},\{E_i\})\rangle$ can be written as the multidimensional convolution ($\cdot$ symbol)

$$\langle\Gamma(t_\mathrm{L},\{E_i\})\rangle = \frac{1}{n}P(t_\mathrm{L},\{E_i\})\cdot\rho_n(t_\mathrm{L},\{E_i\}), \qquad (1)$$

between the n-body phase-space density $\rho_n(\{t_{0,i}\},\{E_{0,i}\})$ and the IELS slicing function $P(\{t_{0,i}\},\{E_{0,i}\}) = \prod_{i=1}^{n}\Gamma(t_\mathrm{L}-t_{0,i},E_i-E_{0,i})$ over the delay times $\{t_{0,i}\}$ and energies $\{E_{0,i}\}$ of the electrons entering the IELS scattering region (see End Matter).

We begin characterizing the few-electron states by acquiring pump-probe spectrograms [Fig. 2(a)]. A nanometer-sized electron beam is focused onto a silicon membrane (see End Matter). Femtosecond laser pulses generate an optical near field at the membrane with photon energy $\hbar\omega_\mathrm{L} = 1.72$ eV that scatters the traversing electrons with an electron-light coupling strength $|\beta| = 5.8$. Delay scans sorted by the electron number in the pulse are shown in Figs. 2(b)–2(d). At large delays, we identify characteristic single-, double- and triple-lobed spectra for $n = 1$–3 [8]. Near temporal overlap, electrons undergo inelastic scattering to higher and lower energies, depleting the zero-loss peak. This is evident in the plots of delay-dependent spectral change [Figs. 2(e)–2(g)], obtained by subtracting the delay-dependent spectra from the spectra at large delays. We identify single-, double-, and triple-peaked regions for number states $n = 1$–3, showing different arrival times of the electrons within a state at the sample plane, as observed in streaking experiments [40].

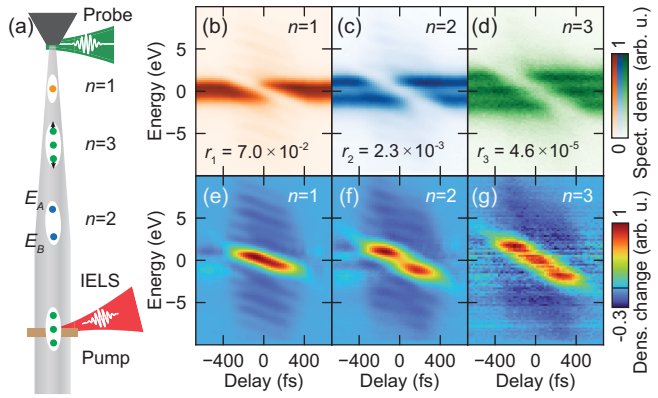


FIG. 2. Inelastic electron-light scattering of few-electron pulses. (a) Coulomb-correlated electron pulses traverse a time-delayed optical near field at a silicon membrane, undergoing inelastic electron-light scattering. (b)–(d) Pump-probe delay scans of pulse charge-resolved components $n = 1$–3. (e)–(g) Delay-dependent spectral change reveals the temporal separation of electrons within a pulse.

For quantitative analysis, we consider electrons scattered to high-order sidebands near the laser peak intensity. This approach can be adopted to any number of electrons with a well-defined energy separation. Here, we investigate two-electron pulses exhibiting a spectral double-lobe with a 1.8 eV energy gap between the electrons, visible in the pair correlation histogram [Fig. 3(a)]. The use of a single pump pulse in the IELS experiment, providing one single reference time t_L, prevents the full reconstruction of the multiparticle correlations through $\rho_n(\{t_i\},\{E_i\})$ [see Eq. (1)]. However, its marginal $\rho_n(t,E)$ is accessible, as detailed below.

Experimentally, predominantly one of the two electrons undergoes IELS at any given delay due to the sufficient temporal separation of the energetically separated electrons. We assign E_A to the initially slower (later-arriving) electron and E_B to the faster one. An optical near field at pump-probe delay t_L selectively scatters either electron, as exemplified for $t_L = -100$ fs [Fig. 3(b), upper panel] and $t_L = 100$ fs [Fig. 3(c), upper panel], respectively. Pair density maps of the two measured energies E_1 and E_2 after the interaction illustrate the selective interaction with the initially faster or slower electron [lower panels of Figs. 3(b) and 3(c)]. In both cases, electrons are scattered along the E_1 and E_2 axes, but the so-generated IELS combs exhibit delay-dependent offsets. Specifically, the green and pink open-ended rectangles define selective electron-gain-scattering filters for the faster and slower electron, respectively. These filters are used to extract energy- and delay-dependent densities shown in Fig. 3(d). The gain contributions are temporally separated, but overlap to some extent at small delays. Assuming laser-pulse durations are short compared to the electron pulse profile, this procedure links the different contributions forming the two-dimensional phase-space density $\rho_2(t,E) = \rho_A(t,E) + \rho_B(t,E)$ to the relative intensities I_A (pink) and I_B (green) of the filtered spectrograms, now expressed by the convolutions

$$I_{A/B}(t_L,E_2) \approx \frac{1}{2}\Gamma(t_L,E_2)\cdot\rho_{A/B}(t_L,E_2), \tag{2}$$

(see End Matter and Refs. [35,36,53,60]). Therefore, the data analysis required to obtain ρ_2 simplifies to a deconvolution of Eq. (2), carried out by a standard procedure (see End Matter and Supplemental Material SM [61]).

The phase-space densities of the single and double-electron pulses shown in Fig. 4 are clearly distinct. While the single-electron distribution exhibits one lobe, the two-electron pulse distribution is bimodal with two regions

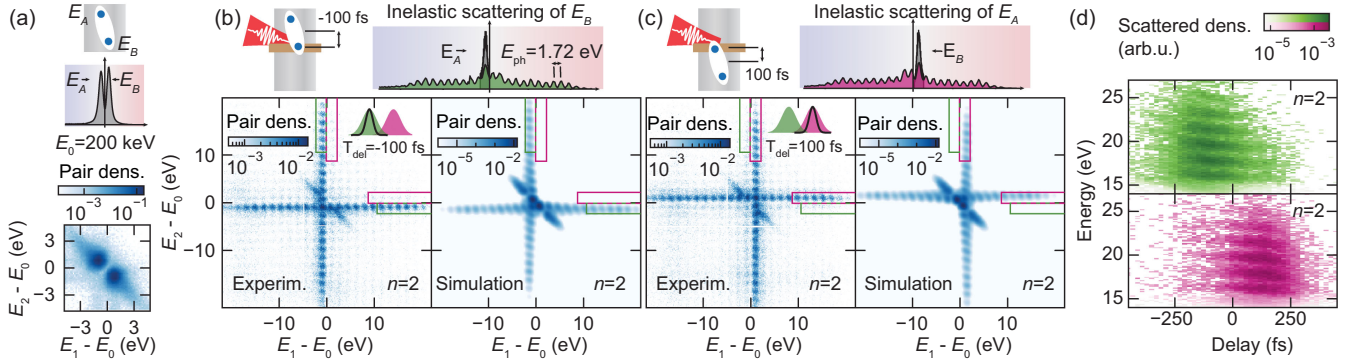


FIG. 3. Phase-space reconstruction of double-electron states via inelastic electron-light scattering (IELS). (a) Scheme (top), spectrum (middle) and energy pair histogram (bottom) of the bare Coulomb correlated $n = 2$-state at $r_2 = 1.1 \times 10^{-4}$. (b),(c) Top: selective scattering of the faster (b) or the slower electron (c) by a time-delayed optical near field. Bottom: pair histograms of measured energies $E_{1/2}$ for coincident electrons A (slower, energy E_A) and B (faster, energy E_B) at pump-probe delays of -100 fs (b) and 100 fs (c) along with corresponding simulations. Green and pink rectangles mark the first and second electrons' energy gain regions, respectively. (d) Gain-filtered IELS spectra of faster (green) and slower (pink) electrons.

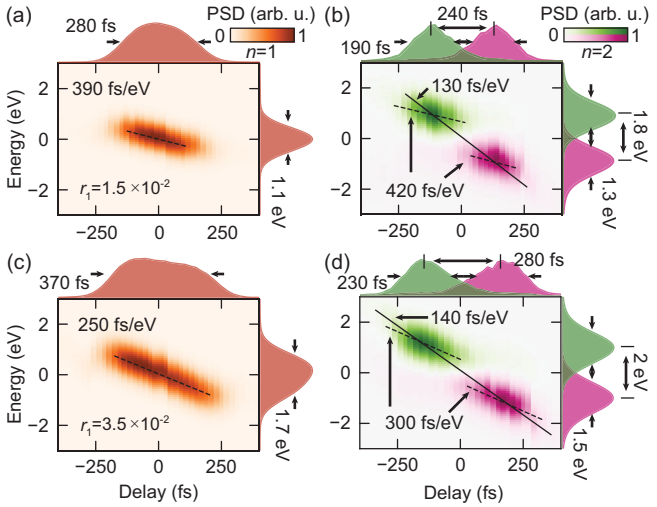


FIG. 4. Reconstructed marginalized phase-space densities of single- (a),(c) and double-electron states (b),(d) at the sample plane for electron rates $r_1 = 1.5 \times 10^{-2}$, $r_2 = 1.1 \times 10^{-4}$ (a),(b) and $r_1 = 3.5 \times 10^{-2}$, $r_2 = 5.6 \times 10^{-4}$ (c),(d). The dashed lines show linear fits, indicating a single-electron pulse chirp of 390 fs/eV and 250 fs/eV for the two cases. Subensemble fits in (b) and (d) yield reduced chirps of 420 fs/eV (b) and 300 fs/eV (d) while the slopes between the phase-space distribution maxima (solid lines) are 130 fs/eV (b) and 140 fs/eV (d).

spectrally and temporally separated by 1.8 eV and 240 fs, respectively [Figs. 4(a) and 4(b)]. Tailoring the photoemission pulse duration allows control over the temporal separation of the electrons at the sample plane (see SM [61]). In general, the phase-space densities are affected by mean-field and stochastic interaction close to the emitter [35,36], resulting in an electron pulse chirp that depends on the current and is also affected by scattering with electrons not entering the beam (compare the upper and lower panels in Fig. 4). We find a similar chirp and current-dependent change thereof for the phase-space distribution of single-electron pulses and the subensembles constituting the two-electron pulse. This chirp decreases from a value around 400 fs/eV at lower current to near or below 300 fs/eV at higher current. In contrast, the two separate lobes of the two-electron distribution exhibit an effective chirp of 130–140 fs/eV that only weakly depends on the photocurrent [solid lines in Figs. 4(b) and 4(d)]. This weak dependence on laser power illustrates that Coulomb correlations are largely unaffected by stochastic interactions with electrons not entering the beam, as the correlation gap varies little with the photoelectron rate [8]. Moreover, the lower chirp value between the two lobes compared to that within the subensembles reflects that the energy difference of the electrons emerges during propagation. This, in turn, causes reduced dispersion as compared to that experienced by variations in initial conditions upon photoemission. We note that these features of the experimentally retrieved longitudinal phase-space distributions of double-electron states are also reproduced by the trajectory simulations discussed in Fig. 1(b). Considering further details of the reconstructed two-electron densities, we recognize a nonlinear distortion, flattening towards zero delay and increasing towards larger absolute delays. This higher-order chirp [cf. Figs. 4(b) and 3(d)] suggests a correlation of the final electron energy difference with the remaining dispersion during propagation: stronger scatterings tend to occur closer to the emitter, leaving a larger influence of dispersion after the interaction, whereas weaker interactions coincide with lower total dispersion.

To actively shape the two-electron time-energy correlations, we extend our scheme beyond the short-pulse regime. So far, we have used IELS with laser pulses shorter than the single-electron ensemble duration for phase-space characterization. To achieve coherent phase modulation [57] across the entire ensemble, we now apply IELS with a much longer pulse ($\Delta_L \approx 2$ ps), imprinting a fixed optical phase onto both electrons. Figure 5(a) shows the resulting phase modulation at a photon energy $\hbar\omega_L = 2$ eV and varying modulation strength. We observe a checkerboard density pattern from a two-particle quantum walk, matching simulations of classically (nonentangled) correlated electrons [Fig. 5(b) and End Matter]. Unlike the short-pulse IELS case [Figs. 3(b) and 3(c)], here, the full ensemble interacts with a field with fixed amplitude and phase over multiple optical cycles, producing multipath interference of measured sidebands [57] and strong population of high-order scattering for both electrons [Fig. 5(a)].

The coherent interaction with the IELS field synchronously shapes the two-electron pulse so that each pair of final kinetic energies shows a distinct temporal correlation atop the Coulomb-induced repulsion [Fig. 5(c)]. This is illustrated by the two-electron Wigner function after the IELS stage, shown in the upper panel of Fig. 5(d) at fixed post-interaction energy (E_1, E_2). By convoluting the pair Wigner function's time coordinates, we derive a quasiprobability (see End Matter) representing the electron current versus the time difference $\Delta t = t_1 - t_2$ and selected final energies, marked by matching symbols in Figs. 5(e) and 5(f). Electrons postselected on the gain side show a quasiprobability peaked at Δt values that are integer multiples of the laser period, while gain-loss combinations yield maxima offset by half an optical cycle. Both features stem from subcycle energy-time correlations optically imprinted on each electron. A dual-frequency arrival-time correlation appears when one electron is selected near an unscattered sideband.

Such attosecond interparticle correlations can be leveraged to coherently act on nanoscale systems in a manner controlled by the final postselected energies. For instance, the probability of detecting a free photon with energy $\hbar\omega_{CL}$, emitted when two-modulated electrons at final energies E_1 and E_2 interact with a second cathodoluminescence

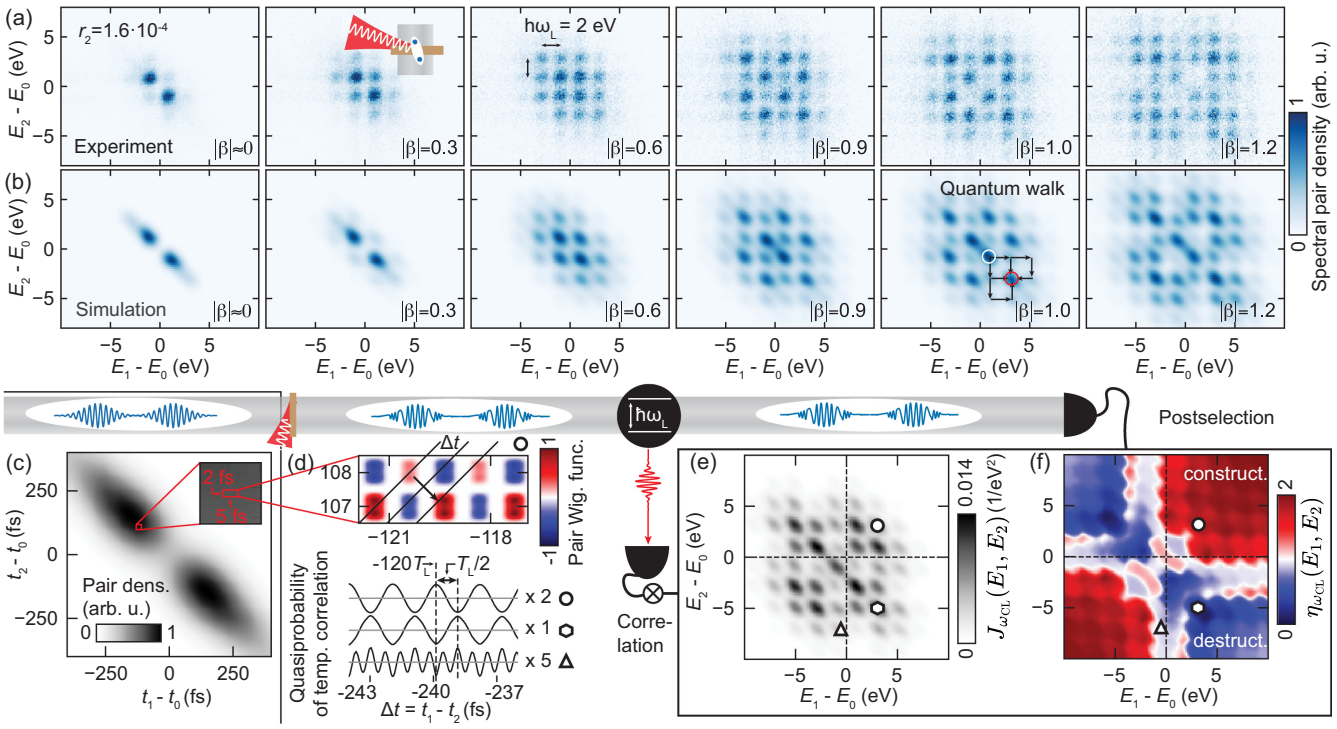


FIG. 5. Coherent shaping of two-electron pulses enables attosecond interparticle correlations and coherent modulation of electron-light coupling. (a),(b) Experimental (a) and simulated (b) spectral pair histograms of $E_{1/2} - E_0$ after long pulse IELS for increasing $|\beta|$ at $r_2 = 1.6 \times 10^{-4}$ and $\Delta_L \approx 2$ ps. (c)–(f) Concept for coherent multiparticle excitation of quantum systems. (c) Simulated temporal pair histogram at the sample plane. (d) Top: IELS-shaped two-electron Wigner function $W(t_1, t_2, E_1 + \hbar\omega_L/2, E_2 + \hbar\omega_L/2)$ (see End Matter) at postselection energy $(E_1 - E_0, E_2 - E_0) = (1.5, 1.5)\hbar\omega_L$ (circle) in the region indicated by the close-up view. Bottom: quasiprobability of the electron-electron delay $W_{\omega_L}(\Delta t, E_1, E_2)$ obtained from the time-convolution of the two-electron Wigner function (see scheme in the upper panel and End Matter) for postselection energies $(1.5, -2.5)\hbar\omega_L$ (hexagon), and $(-0.5, -3.5)\hbar\omega_L$ (triangle). (e),(f) Interaction of two electrons with a second specimen excited at frequency ω_L followed by the emission of a CL photon at equal energy (see sketch). Two-electron postselection in coincidence with the CL photon forms the correlation signal [see Eq. (3)] and consists of an incoherent contribution $2P_{CL}J_{\omega_L}$ (e) and a coherent modulation η_{ω_L} (f).

(CL)-emitting sample (e.g., generating transition or Cherenkov radiation [56]), is given by (see End Matter)

$$P_{\omega_{CL}}(E_1, E_2) = 2P_{CL}J_{\omega_{CL}}(E_1, E_2)\eta_{\omega_{CL}}(E_1, E_2). \quad (3)$$

This includes an incoherent part $2P_{CL}J_{\omega_{CL}}$ and a coherent modulation $\eta_{\omega_{CL}}$. In Figs. 5(e) and 5(f), both are computed for the two-electron states in Fig. 5(b), with $\omega_{CL} = \omega_L$ and $|\beta| \approx 1.2$. The incoherent term multiplies the uncorrelated photon-emission probability $2P_{CL}$ by the normalized energy density $J_{\omega_{CL}}$ counting the electron pairs compatible with the transition [Fig. 5(e)]. The coherent factor stems from IELS-induced energy-dependent subcycle timing correlations, which enhance or suppress CL emission through interference in the total exciting field [Fig. 5(f)], and directly relates to the Wigner functions in Fig. 5(d).

Without postselection, the associated probability—obtained by integrating Eq. (3) over the full energy domain—follows the superradiant scaling $2P_{CL}(1 + \mathrm{DOC}_{\omega_{CL}})$, which depends on the so-called degree of coherence $0 \leq \mathrm{DOC}_{\omega_{CL}} \leq 1$ [17,21,22]. In particular, ensembles bunched through a combination of IELS modulation stages and free spatial drift yield a nonzero degree of coherence, whereas uncompressed ensembles show a vanishing $\mathrm{DOC}_{\omega_{CL}}$ [62,63]. In this regard, excitation control through postselection relaxes spatial constraints between the IELS stage and the target system and enables a broader range of modulations, including emission suppression.

In summary, we map Coulomb-induced femtosecond-electronvolt splitting in multielectron phase-space distributions and predict attosecond temporal correlations in an ultrafast transmission electron microscope. To reconstruct femtosecond phase-space electron correlations, we extend the theoretical framework of quantum inelastic electron-light interaction to multielectron states, incorporating classical ensembles averaging. In particular, we obtain the marginals of the n-particle phase-space distribution by filtering the gain part of the single-pulse IELS spectrum associated with each electron [see Eq. (2)]. We find that electrons emitted by the same laser pulse mutually exchange energy over centimeter-scale acceleration distances, thereby

acquiring arrival time separations on the order of $\approx$ 200 fs at the sample plane. Future studies employing n femtosecond-separated laser pulses with adjustable delays will address the reconstruction of the full longitudinal n-electron phase-space distribution $\rho_n(\{t_i\},\{E_i\})$, provided that the energy gap exceeds the spectral resolution. By extending the duration of the IELS modulation, we imprint a coherent optical phase onto the entire multielectron ensemble. We theoretically show that the resulting multielectron quantum walk can be employed to coherently control optical excitations in material systems without dispersive bunching. More broadly, the framework of inelastic few-electron-light scattering opens various opportunities to modulate and control electron number states using light pulses tailored to the densities of the individual electrons and utilize density modulation to induce superradiance in bosonic or fermionic quantum systems.

Acknowledgments—We acknowledge the continued support from the Göttingen UTEM team. We thank Thomas Rittmann for insightful discussions on phase-space density reconstruction. The experiments were conducted at the Göttingen UTEM Lab, funded by the Deutsche Forschungsgemeinschaft (German Research Foundation) through Project-ID 432680300 (SFB 1456, project C01 to C. R.), the Gottfried Wilhelm Leibniz program (RO 3936/4-1 to C. R.) and the European Union's Horizon 2020 research and innovation programme under Grant Agreement No. 101017720 (FET-Proactive EBEAM). During the review stage of this manuscript, a preprint of related two-electron IELS experiments was posted [64], and we acknowledge fruitful discussions with the authors.

C. R. directed the study. R. H. conducted the experiments and data analysis with contributions from A. F. R. H. prepared the figures, with contributions from V. D. G., R. H. and V. D. G. conducted particle simulations. V. D. G. developed the theoretical framework. All authors discussed the results and interpretation. R. H., V. D. G., and C. R. wrote the manuscript with input and feedback from A. F.

The authors declare no competing financial interests.

Data availability—The data that support the findings of this article are openly available [65].

[1] H. Boersch, Z. Phys. **139**, 115 (1954).
[2] K. H. Loeffler, Z. Angew. Phys. **27**, 145 (1969).
[3] S. Borrelli, T. C. H. de Raadt, S. B. van der Geer, P. H. A. Mutsaers, K. A. H. van Leeuwen, and O. J. Luiten, Phys. Rev. Lett. **132**, 115001 (2024).
[4] H. Kiesel, A. Renz, and F. Hasselbach, Nature (London) **418**, 392 (2002).
[5] T. Kodama, N. Osakabe, and A. Tonomura, Phys. Rev. A **83**, 063616 (2011).
[6] M. Kuwahara, Y. Yoshida, W. Nagata, K. Nakakura, M. Furui, T. Ishida, K. Saitoh, T. Ujihara, and N. Tanaka, Phys. Rev. Lett. **126**, 125501 (2021).
[7] S. Keramati, W. Brunner, T. J. Gay, and H. Batelaan, Phys. Rev. Lett. **127**, 180602 (2021).
[8] R. Haindl, A. Feist, T. Domröse, M. Möller, J. H. Gaida, S. V. Yalunin, and C. Ropers, Nat. Phys. **19**, 1410 (2023).
[9] P. Hommelhoff, Y. Sortais, A. Aghajani-Talesh, and M. A. Kasevich, Phys. Rev. Lett. **96**, 077401 (2006).
[10] C. Ropers, D. R. Solli, C. P. Schulz, C. Lienau, and T. Elsaesser, Phys. Rev. Lett. **98**, 043907 (2007).
[11] B. Barwick, C. Corder, J. Strohaber, N. Chandler-Smith, C. Uiterwaal, and H. Batelaan, New J. Phys. **9**, 142 (2007).
[12] S. Meier, J. Heimerl, and P. Hommelhoff, Nat. Phys. **19**, 1402 (2023).
[13] S. A. Koppell, J. W. Simonaitis, M. A. R. Krielaart, W. P. Putnam, K. K. Berggren, and P. D. Keathley, New J. Phys. **27**, 023012 (2025).
[14] A. Gover and A. Yariv, Phys. Rev. Lett. **124**, 064801 (2020).
[15] Z. Zhao, X.-Q. Sun, and S. Fan, Phys. Rev. Lett. **126**, 233402 (2021).
[16] A. Karnieli, N. Rivera, A. Arie, and I. Kaminer, Phys. Rev. Lett. **127**, 060403 (2021).
[17] F. J. García de Abajo and V. Di Giulio, ACS Photonics **8**, 945 (2021).
[18] D. Rätzel, D. Hartley, O. Schwartz, and P. Haslinger, Phys. Rev. Res. **3**, 023247 (2021).
[19] B. Zhang, D. Ran, R. Ianconescu, A. Friedman, J. Scheuer, A. Yariv, and A. Gover, Phys. Rev. Lett. **126**, 244801 (2021).
[20] R. Ruimy, A. Gorlach, C. Mechel, N. Rivera, and I. Kaminer, Phys. Rev. Lett. **126**, 233403 (2021).
[21] O. Kfir, V. Di Giulio, F. J. G. de Abajo, and C. Ropers, Sci. Adv. **7**, eabf6380 (2021).
[22] V. Di Giulio, O. Kfir, C. Ropers, and F. J. García de Abajo, ACS Nano **15**, 7290 (2021).
[23] A. Gorlach, O. Reinhardt, A. Pizzi, R. Ruimy, G. Baranes, N. Rivera, and I. Kaminer, Phys. Rev. A **109**, 023722 (2024).
[24] V. Di Giulio, R. Haindl, and C. Ropers, Nanophotonics **14**, 1865 (2025).
[25] E. J. VandenBussche and D. J. Flannigan, Nano Lett. **19**, 6687 (2019).
[26] J. J. Axelrod, J. T. Zhang, P. N. Petrov, R. M. Glaeser, and H. Müller, Curr. Opin. Struct. Biol. **86**, 102805 (2024).
[27] O. Kfir, Phys. Rev. Lett. **123**, 103602 (2019).
[28] N. Talebi and I. Březinová, New J. Phys. **23**, 063066 (2021).
[29] A. Konečná, F. Iyikanat, and F. J. García de Abajo, Sci. Adv. **8**, eabo7853 (2022).
[30] E. Kazakevich, H. Aharon, and O. Kfir, Phys. Rev. Res. **6**, 043033 (2024).
[31] J.-W. Henke, H. Jeng, and C. Ropers, Phys. Rev. A **111**, 012610 (2025).
[32] A. Preimesberger, S. Bogdanov, I. C. Bicket, P. Rembold, and P. Haslinger, arXiv:2504.13163.
[33] J.-W. Henke, H. Jeng, M. Sivis, and C. Ropers, arXiv:2504.13047.
[34] A. H. Zewail, Science **328**, 187 (2010).
[35] A. Feist, N. Bach, N. Rubiano da Silva, T. Danz, M. Möller, K. E. Priebe, T. Domröse, J. G. Gatzmann, S. Rost, J. Schauss, S. Strauch, R. Bormann, M. Sivis, S. Schäfer, and C. Ropers, Ultramicroscopy **176**, 63 (2017).

[36] N. Bach, T. Domröse, A. Feist, T. Rittmann, S. Strauch, C. Ropers, and S. Schäfer, Struct. Dyn. **6**, 014301 (2019).
[37] P. K. Olshin, M. Drabbels, and U. J. Lorenz, Struct. Dyn. **7**, 054304 (2020).
[38] C. Zhu, D. Zheng, H. Wang, M. Zhang, Z. Li, S. Sun, P. Xu, H. Tian, Z. Li, H. Yang, and J. Li, Ultramicroscopy **209**, 112887 (2020).
[39] R. Shiloh, T. Chlouba, and P. Hommelhoff, Phys. Rev. Lett. **128**, 235301 (2022).
[40] J. Kuttruff, D. Nabben, A.-C. Zimmermann, A. Ryabov, and P. Baum, Sci. Adv. **10**, eadl6543 (2024).
[41] A. Schröder, A. Wendeln, J. T. Weber, M. Mukai, Y. Kohno, and S. Schäfer, Ultramicroscopy **275**, 114158 (2025).
[42] D. H. Dowell and J. F. Schmerge, Phys. Rev. ST Accel. Beams **12**, 074201 (2009).
[43] B. Cook, M. Bronsgeest, K. Hagen, and P. Kruit, Ultramicroscopy **109**, 403 (2009).
[44] G. Herink, D. R. Solli, M. Gulde, and C. Ropers, Nature (London) **483**, 190 (2012).
[45] M. Krüger, M. Schenk, and P. Hommelhoff, Nature (London) **475**, 78 (2011).
[46] G. Hergert, R. Lampe, A. Wöste, and C. Lienau, Nano Lett. **24**, 11067 (2024).
[47] B. Cook and P. Kruit, Appl. Phys. Lett. **109**, 151901 (2016).
[48] M. Kuwahara, Y. Nambo, K. Aoki, K. Sameshima, X. Jin, T. Ujihara, H. Asano, K. Saitoh, Y. Takeda, and N. Tanaka, Appl. Phys. Lett. **109**, 013108 (2016).
[49] S. Meier and P. Hommelhoff, ACS Photonics **9**, 3083 (2022).
[50] C. T. Hebeisen, G. Sciaini, M. Harb, R. Ernstorfer, T. Dartigalongue, S. G. Kruglik, and R. J. D. Miller, Opt. Express **16**, 3334 (2008).
[51] M. Kozák, J. McNeur, K. J. Leedle, H. Deng, N. Schönenberger, A. Ruehl, I. Hartl, J. S. Harris, R. L. Byer, and P. Hommelhoff, Nat. Commun. **8**, 14342 (2017).
[52] D. Epp, B. Schröder, M. Möller, and C. Ropers, Struct. Dyn. **11**, 024306 (2024).
[53] S. T. Park, O.-H. Kwon, and A. H. Zewail, New J. Phys. **14**, 053046 (2012).
[54] F. O. Kirchner, A. Gliserin, F. Krausz, and P. Baum, Nat. Photonics **8**, 52 (2014).
[55] B. Barwick, D. J. Flannigan, and A. H. Zewail, Nature (London) **462**, 902 (2009).
[56] F. J. García de Abajo, Rev. Mod. Phys. **82**, 209 (2010).
[57] A. Feist, K. E. Echternkamp, J. Schauss, S. V. Yalunin, S. Schäfer, and C. Ropers, Nature (London) **521**, 200 (2015).
[58] R. Ballabriga, M. Campbell, and X. Llopart, Nucl. Instrum. Methods Phys. Res., Sect. A **878**, 10 (2018).
[59] J. P. van Schayck, E. van Genderen, E. Maddox, L. Roussel, H. Boulanger, E. Fröjdh, J.-P. Abrahams, P. J. Peters, and R. B. Ravelli, Ultramicroscopy **218**, 113091 (2020).
[60] D. A. Plemmons, S. Tae Park, A. H. Zewail, and D. J. Flannigan, Ultramicroscopy **146**, 97 (2014).
[61] See Supplemental Material at http://link.aps.org/supplemental/10.1103/lylq-m63c for additional information on the theoretical treatment of multielectron CL and long-pulse IELS, the influence of experimental parameters on the phase-space correlations and the experimental two-electron phase-space density reconstruction.
[62] S. V. Yalunin, A. Feist, and C. Ropers, Phys. Rev. Res. **3**, L032036 (2021).
[63] F. J. García de Abajo and C. Ropers, Phys. Rev. Lett. **130**, 246901 (2023).
[64] O. Tziperman, D. Nabben, R. Ruimy, J. Holder, E. Nussinson, Y. Fang, A. Gorlach, D. Kazenwadel, A. Karnieli, I. Kaminer, and P. Baum, arXiv:2505.03707.
[65] R. Haindl, V. Di Giulio, A. Feist, and C. Ropers, Edmond, 10.17617/3.MJO3RE (2025).
[66] S. T. Park, M. Lin, and A. H. Zewail, New J. Phys. **12**, 123028 (2010).
[67] F. J. García de Abajo, A. Asenjo-Garcia, and M. Kociak, Nano Lett. **10**, 1859 (2010).
[68] S. T. Park and A. H. Zewail, J. Phys. Chem. A **116**, 11128 (2012).
[69] G. M. Vanacore, I. Madan, G. Berruto, K. Wang, E. Pomarico, R. J. Lamb, D. McGrouther, I. Kaminer, B. Barwick, F. J. García de Abajo, and F. Carbone, Nat. Commun. **9**, 2694 (2018).
[70] M. Abramowitz and I. A. Stegun, *Handbook of Mathematical Functions* (Dover, New York, 1972).
[71] E. Wigner, Phys. Rev. **40**, 749 (1932).

End Matter

Trajectory simulations—Few-electron phase-space distributions are simulated via relativistic particle trajectory simulations. We numerically solve the equations of motion for particles mutually interacting via Coulomb's force in a static electric field

$$\frac{\mathrm{d}\mathbf{p}_i(t)}{\mathrm{d}t} = \frac{e^2}{4\pi\varepsilon_0}\sum_{j\neq i}^{n}\frac{\mathbf{r}_i-\mathbf{r}_j}{|\mathbf{r}_i-\mathbf{r}_j|^3} + e\mathbf{E}_{\mathrm{static}}(\mathbf{r}_i), \quad \text{(A1)}$$

where $\mathbf{p}_i$, $\mathbf{r}_i$, e and m_e are the relativistic momentum, position, charge, and rest mass of the ith electron. Their momentum follows $\mathbf{p}_i = \gamma m_\mathrm{e}\mathbf{v}_i = m_\mathrm{e}\mathbf{v}_i/\sqrt{1-v_i^2/c^2}$. The electrons are accelerated by a static two-stage field $\mathbf{E}_{\mathrm{static}}(\mathbf{r}_i) = \mathbf{E}_{\mathrm{ext}}(\mathbf{r}_i) + \mathbf{E}_{\mathrm{acc}}(\mathbf{r}_i)$. The nonlinear extraction field is $\mathbf{E}_{\mathrm{ext}}(\mathbf{r}) = U_{\mathrm{ext}}\mathbf{r}/r^3(r_{\mathrm{tip}}^{-1} - R_{\mathrm{ext}}^{-1})$ with extraction voltage $U_{\mathrm{ext}} = 2$ kV, tip radius $r_{\mathrm{tip}} = 1$ μm, and the distance between tip and extractor $R_{\mathrm{ext}} = 500$ μm. The constant axial field is $\mathbf{E}_{\mathrm{acc}}(\mathbf{r}) = U_{\mathrm{acc}}\hat{\mathbf{z}}/d_{\mathrm{acc}}$ if $z \leq d_{\mathrm{acc}}$, with the acceleration voltage $U_{\mathrm{acc}} = 198$ kV and accelerating distance $d_{\mathrm{acc}} = 0.85$ m. For each simulation run, the electrons are randomly distributed on a 1 μm-sized spherical tip over an area with radius 170 nm. The finite laser pulse length and distribution of initial electron energy are modeled via normal distributions of start times and velocities with standard deviations $\sigma_{0,t} =$ 80 fs and $\sigma_{0,E} = 0.35$ eV. The ratio between initial longitudinal $v_\parallel$ and transverse v_{trans} velocity components

$v_\perp/v_\parallel$ is given by $\tan(\theta)$, where θ is defined with respect to the tip surface normal at the place of emission and is uniformly distributed between $-2°$ and $2°$. Finally, finite spectrometer resolution and high-voltage stability are included via incoherent temporal and spectral averaging with standard deviations $\sigma_{0,t} = 30$ fs and $\sigma_{0,E} = 0.13$ eV.

Experimental details—The photoemission laser operates at a photon energy of 2.4 eV, delivering pulses with a duration of 160 fs at a repetition rate of 2 MHz. For near-field generation at a 35 nm-thick silicon membrane, we use femtosecond laser pulses with a photon energy of 1.72 eV, a full-width-at-half-maximum intensity duration of $1.67\Delta_\mathrm{L} \approx 120$ fs, and peak intensities of 11 GW/cm^2. IELS is performed with electron-laser and electron-sample angles of $\theta_\mathrm{el/las} = 55°$ and $\theta_\mathrm{el/sam} = 10°$, respectively, where the laser and electron beam directions are coplanar to the surface normal.

Multielectron IELS theory for short laser pulses—Theoretical modeling of the energy correlation maps in the main text requires an extension of the established IELS framework [66–69] for electrons at kiloelectronvolt energies to n electrons. Here, the minimal coupling Hamiltonian for n swift electrons with velocities $\{\mathbf{v}_i\}$ interacting with a classical time-varying vector potential $\mathbf{A}(\mathbf{r},t)$ is simplified by linearizing the electrons' dispersion relation around a central momentum $\mathbf{k}_0$, taken to be the average momentum and corresponding to the relativistic energy $E_0 = c\sqrt{m_\mathrm{e}^2c^2 + \hbar^2k_0^2}$ and velocity $\mathbf{v} = (\hbar c^2/E_0)\mathbf{k}_0$. Neglecting spin flips, ponderomotive forces, small velocity differences of the order $|\mathbf{v} - \mathbf{v}_i|/c \sim 10^{-5}$ between electrons, and Coulomb repulsion close to the Si membrane, we can solve the Schrödinger equation $\mathrm{i}\hbar\partial_t\psi^i(\mathbf{r}_i,t) = \mathcal{H}^i\psi^i(\mathbf{r}_i,t)$ for each ith electron separately with Hamiltonian $\mathcal{H}^i = E_0 - \hbar\mathbf{v}\cdot(\mathrm{i}\nabla_{\mathbf{r}_i} + \mathbf{k}_0) + (e\mathbf{v}/c)\cdot\mathbf{A}(\mathbf{r}_i,t)$, which admits the analytical solution

$$\psi^i(\mathbf{r}_i,t) = \psi_0^i(\mathbf{r}_i,t) \times \exp\left\{(-\mathrm{i}e/\hbar c)\int_{-\infty}^{t} dt'\,\mathbf{v}\cdot\mathbf{A}[\mathbf{r}_i - \mathbf{v}(t-t'),t']\right\} \tag{C1}$$

for an initial wave function $\psi_0^i(\mathbf{r}_i,t) = \mathrm{e}^{\mathrm{i}(\mathbf{k}_0\cdot\mathbf{r}_i - E_0t/\hbar)} \times \phi_0^i(\mathbf{r}_i - \mathbf{v}t)$ entering the interaction zone. By treating each electron independently, we implicitly neglect quantum correlations, i.e., entanglement, in the beam. This assumption is justified by arguing that stochastic interaction with electrons that are not coupled into the column will likely wash out any Coulomb-induced coherent correlation, whose preservation would require a redesign of the photoemission and propagation process beyond current capabilities. Furthermore, an analysis similar to Ref. [64] of the data from Fig. 5(a) reveals no two-particle longitudinal energy entanglement at the sample plane.

We now consider a semi-monochromatic laser pulse at frequency ω_L with a vector potential that is described by a slowly varying electric-field envelope with a negligible time derivative $\vec{\mathcal{E}}(\mathbf{r},t)$ as $\mathbf{A}(\mathbf{r},t) = (-\mathrm{i}c/\omega_\mathrm{L})\vec{\mathcal{E}}(\mathbf{r},t)\mathrm{e}^{-\mathrm{i}\omega_\mathrm{L}t} + \mathrm{c.c.}$ Equation (C1) can then be reformulated via a superposition of amplitudes corresponding to gain and loss of ℓ light quanta (gain: $\ell > 0$, loss: $\ell < 0$) for each electron using the Jacobi-Anger expansion $\mathrm{e}^{\mathrm{i}u\sin\theta} = \sum_{\ell=-\infty}^{\infty} J_\ell(u)\mathrm{e}^{\mathrm{i}\ell\theta}$ [Eq. (9.1.41) of Ref. [70]]. Thereby, Eq. (C1) transforms into

$$\psi^i(\mathbf{r}_i,t) = \psi_0^i(\mathbf{r}_i,t)\sum_{\ell=-\infty}^{\infty} J_\ell(2|\beta(\mathbf{r}_i,t)|)\mathrm{e}^{\mathrm{i}\ell\varphi(\mathbf{r}_i,t)}, \tag{C2}$$

with $\varphi(\mathbf{r},t) = \arg\{-\beta(\mathbf{r},t)\}$ and the time-dependent coupling coefficient $\beta(\mathbf{r},t) = (e/\hbar\omega_\mathrm{L})\int_{-\infty}^{t} dt'\mathbf{v}\cdot\vec{\mathcal{E}}[\mathbf{r} - \mathbf{v}(t-t'),t']\mathrm{e}^{-\mathrm{i}\omega_\mathrm{L}t'}$. Assuming electron propagation along the z axis and sample arrival time t_L of a Gaussian laser with profile $\vec{\mathcal{E}}(\mathbf{r},t) = \vec{\mathcal{E}}(\mathbf{r})\mathrm{e}^{-(t-t_\mathrm{L})^2/2\Delta_\mathrm{L}^2}$, and given the short laser pulses (tens of fs), electron coherence times (few fs), and interaction times (sub-fs) used in this Letter, we approximate $\beta(\mathbf{r},t) \approx \mathrm{e}^{-[z/v-(t-t_\mathrm{L})]^2/2\Delta_\mathrm{L}^2 - \mathrm{i}\omega_\mathrm{L}(t-z/v)}\beta$ with $\beta = (e/\hbar\omega_\mathrm{L})\int_{-\infty}^{z} dz'\mathcal{E}_z(\mathbf{R},z')\mathrm{e}^{-\mathrm{i}\omega_\mathrm{L}z'/v}$. By plugging $\beta(\mathbf{r},t)$ into Eq. (C2), we obtain

$$\psi^i(\mathbf{r}_i,t) = \psi_0^i(\mathbf{r}_i,t)\mathcal{P}(\mathbf{R}_i, z_i - vt)$$

where the IELS amplitude $\mathcal{P}(\mathbf{R},z) = \sum_{\ell=-\infty}^{\infty} J_\ell \times [2\mathrm{e}^{-(z/v+t_\mathrm{L})^2/2\Delta_\mathrm{L}^2}|\beta|]\mathrm{e}^{\mathrm{i}\ell(\omega_\mathrm{L}z/v+\varphi)}$ and $\varphi = \arg\{-\beta\}$. The probability $P(\{E_i\}) = \prod_i \Gamma_i(E_i)$ of measuring the n electrons in a set of energies $\{E_i\}$ is directly connected to their wave functions via the one-dimensional spatial Fourier transform $\Gamma_i(E_i) = (1/2\pi\hbar v)\int d\mathbf{R}\left|\int_{-\infty}^{\infty} dz\psi^i(\mathbf{r},t)\,\mathrm{e}^{-\mathrm{i}[k_0+(E_i-E_0)/v\hbar]z}\right|^2$.

For a Gaussian electron of main energy $E_{0,i}$ and coherence time Δ_c, focused around the transversal coordinate $\mathbf{R}_0$, and crossing the interaction plane $z = 0$ at time $t_{0,i}$, we can write $\psi_0^i(\mathbf{r},t) = f(\mathbf{R} - \mathbf{R}_0)\,\mathrm{e}^{\mathrm{i}k_{0,i}z - \mathrm{i}E_{0,i}t/\hbar - (z/v-t+t_{0,i})^2/4\Delta_c^2}/(2\pi v^2\Delta_c^2)^{1/4}$ with $f(\mathbf{R} - \mathbf{R}_0)$ a function satisfying $|f(\mathbf{R} - \mathbf{R}_0)|^2 = \delta(\mathbf{R} - \mathbf{R}_0)$. For such a state, the Fourier transform can be carried out exactly using the expansion $J_\ell(x) = \mathrm{sign}^\ell\ell\sum_{m=0}^{\infty}(-1)^m(x/2)^{2m+|\ell|}/m!(m+|\ell|)!$. The resulting expression can be further simplified by neglecting terms of order $(\Delta_\mathrm{c}/\Delta_\mathrm{L})^4$ and considering $\omega_\mathrm{L}\Delta_c \gg 1$, and is given by $\Gamma_i(E_i) = \Gamma(t_\mathrm{L} - t_{0,i}, E_i - E_{0,i})$ with

$$\Gamma(t,E) = \frac{\Delta_c}{\hbar}\sum_{\substack{\ell=-\infty \\ m,m'=0}}^{\infty} b_{mm'\ell}\mathrm{e}^{-nt^2/\lambda\Delta_\mathrm{L}^2 - 2[E/\hbar - \ell\omega_\mathrm{L}]^2\Delta_\mathrm{c}^2}, \tag{C3}$$

where $\lambda = 1 + 4n\Delta_c^2/\Delta_L^2$, $n = |\ell| + m + m'$, and $b_{mm'\ell} = (-1)^{m+m'}|\beta|^{2n}\sqrt{2}/\sqrt{\pi\lambda}m!m'!(|\ell| + m)!(|\ell| + m')!$.

The recorded energy maps $\langle\Gamma(t_L, \{E_i\})\rangle$ result from an incoherent average (indicated by $\langle\cdot\rangle$) of the n-electron IELS spectra $P(\{E_i\}) = \prod_{i=1}^{n}\Gamma(t_L - t_{0,i}, E_i - E_{0,i})$, acting as a convolution function over the classical $\rho_n(\{t_{0,i}\}, \{E_{0,i}\})$ ensemble of delays $\{t_{0,i}\}$ and energies $\{E_{0,i}\}$ at the sample plane, [see Eq. (1)]. The factor $1/n$ originates from the normalization condition $n = \int\{dt_i\}\{dE_i\}\rho_n(\{t_i\}, \{E_i\})$. In particular, the simulated maps in Figs. 3(b) and 3(c) employ the two-electron phase-space density obtained from the trajectory simulations (see Fig. 1) with parameters $\Delta_L =$ 72 fs, $\Delta_c = 1.29$ fs, and $|\beta| = 5.68$. The coherence time is derived from the spectral width of the nonstochastically broadened single-electron spectrum of $\hbar\sqrt{2\log 2}/\Delta_c \approx 0.6$ eV acquired at very low photoexcitation laser powers [35].

Ensemble averages, such as the one appearing in Eq. (1) and in End Matter *Multi-electron coherent modulation of material excitations*, are computed from the arithmetic mean of the quantities in brackets, evaluated at the time delays $t_{0,i}$ and initial energies $E_{0,i}$ obtained from the Monte Carlo simulations (see End Matter *Trajectory Simulations*). Our simulations provide the required sampling of the relevant phase space, defined by $\rho_n(\{t_i\}, \{E_i\})$, to accurately approximate such averaging integrals.

Slicing and reconstruction algorithm—Because the two electrons are indistinguishable, the two-electron phase-space density $\rho_2(t_1, t_2, E_1, E_2)$ is symmetric under label exchange. Hence, its marginalized distribution can be expressed as $\rho_2(t, E) = \rho_A(t, E) + \rho_B(t, E)$. Coulomb repulsion causes $\rho_A(t, E)$ and $\rho_B(t, E)$ to localize in energy and time around $\bar{E}_A < \bar{E}_B$ and $\bar{t}_A > \bar{t}_B$ (see Fig. 1). The slicing procedure leverages this localization to extract $\rho_A(t, E)$ and $\rho_B(t, E)$ from distinct parts of the spectrograms. Assuming Δ_L is small compared to the temporal separation between ρ_A and ρ_B, integrating the maps $\langle\Gamma(t_L, E_1, E_2)\rangle$ over E_1 for each value of E_2 in the pink (for $t_L \sim \bar{t}_A$) and green (for $t_L \sim \bar{t}_B$) top selection regions of Figs. 3(b) and 3(c) (or equivalently swapping the roles of E_1 and E_2 for the rightmost selection regions), reduces Eq. (1) into the two one-dimensional convolutions reported in Eq. (2).

To obtain the marginalized phase-space densities, we make two other approximations: (i) short laser-pulse duration compared to the temporal distribution widths ($\Delta_L/\sqrt{n} \sim 15$ fs for the outermost energy sidebands); (ii) the energy and time dependencies can be expressed in the form $\rho_{A/B}(t, E) = \alpha_{A/B}(t)e^{-[E - E_{A/B}^{\text{chirp}}(t) - \bar{E}_{A/B}]^2/2\sigma_{\text{inc}}^2}/\sqrt{2\pi\sigma_{\text{inc}}^2}$, i.e., an incoherent Gaussian energy envelope of standard deviation σ_{inc} with chirp function $E_{A/B}^{\text{chirp}}(t)$ multiplied by an unknown time-dependent distribution $\alpha_{A/B}(t)$ is assumed. Substituting into Eq. (2) and using Eq. (C3) in the relevant energy regions, we obtain

$$I_{A/B}(t_L, E_2) \approx \alpha_{A/B}(t_L) \times \sum_{\ell=\ell_{\min}}^{\ell_{\max}} a_\ell e^{-[E_2 - E_{A/B}^{\text{chirp}}(t_L) - \bar{E}_{A/B} - \ell\hbar\omega_L]^2/2\sigma^2}, \quad \text{(D1)}$$

where $\sigma^2 = \hbar^2/4\Delta_c^2 + \sigma_{\text{inc}}^2$ and a_ℓ is a real-valued coefficient, and the summation over ℓ has been limited to the range $[\ell_{\min}, \ell_{\max}]$ to account for the finite number of selected sidebands. Finally, $E_{A/B}^{\text{chirp}}(t)$ is extracted from the phase of the Fourier transform of Eq. (D1), performed along the energy axis and subtracting a constant phase such that $E_{A/B}^{\text{chirp}}(\bar{t}_{A/B}) = 0$, while σ_{inc} is obtained by fitting the envelope of the absolute value of the Fourier transform to a Gaussian function (see SM [61]). The temporal profile $\alpha_{A/B}(t)$ is obtained by integrating Eq. (D1) over E_2 and normalizing the result.

Multielectron coherent modulation of material excitations—To display the energy and time correlations formed from an IELS interaction, we compute the two-electron Wigner function [see Fig. 5(d)]

$$W(t_1, t_2, E_1, E_2) = \langle W_1(t_1, E_1)W_2(t_2, E_2)\rangle, \quad \text{(E1)}$$

obtained by averaging the multiplication of two longitudinal single-electron Wigner functions $W_i(t_i, E_i) = (1/2\pi)\int_{-\infty}^{\infty} dy\psi^{i*}(y/2 - vt_i)\psi^i(-y/2 - vt_i)e^{i[k_0 + (E_i - E_0)/\hbar v]y}$ [71], computed from the $t = 0$ IELS wave function in End Matter *Multielectron IELS theory for short laser pulses*, over the ensemble of delay times and initial energies $\rho_2(t_1, t_2, E_1, E_2)$. For electrons exiting the interaction region and for $\Delta_L/\sigma \gg 1$, we obtain

$$W_i(t_i, E_i) = \frac{1}{\pi}e^{-(t_i - t_{0,i})^2/2\Delta_c^2} \sum_{\ell,\ell'=-\infty}^{\infty} J_\ell(2|\beta|)J_{\ell'}(2|\beta|) \times e^{-2\omega_L^2\Delta_c^2[(E_i - E_{0,i})/\hbar\omega_L - (\ell+\ell')/2]^2} e^{i(\ell-\ell')\omega_L(\varphi/\omega_L - t_i)}, \quad \text{(E2)}$$

which forms the basis for the calculation of Eq. (E1), shown in Fig. 5(d).

In the SM [61], we derive the probability in Eq. (3) of exciting a second sample that, relaxing back to the ground state, emits a CL photon measured at frequency ω_{CL} in coincidence with the detection of an energy pair (E_1, E_2) (see sketch in Fig. 5). Its evaluation requires knowledge of the density of electrons compatible with the CL emission and the energy measurement

$$J_{\omega_{CL}}(E_1, E_2) = \frac{1}{2}\langle PM_0^1(E_1 + \hbar\omega_{CL})PM_0^2(E_2) + PM_0^1(E_1)PM_0^2(E_2 + \hbar\omega_{CL})\rangle \quad \text{(E3)}$$

and of the modulation factor

$$\eta_{\omega_{\mathrm{CL}}}(E_1,E_2) = 1 + \mathrm{Re}\{\langle PM^{1}_{\hbar\omega_{\mathrm{CL}}}(E_1+\hbar\omega_{\mathrm{CL}}/2) \times PM^{2*}_{\hbar\omega_{\mathrm{CL}}}(E_2+\hbar\omega_{\mathrm{CL}}/2)\rangle\}/J_{\omega_{\mathrm{CL}}}(E_1,E_2), \tag{E4}$$

written in terms of the projected coherence factor (PCF) $PM^{i}_{E}(E') = \int_{-\infty}^{\infty} dt\, W_i(t,E')\mathrm{e}^{\mathrm{i}Et/\hbar}/\hbar$ (see Ref. [24] and SM [61]). The product of two Fourier transforms appearing in Eq. (E4) can alternatively be computed from the temporal Fourier transform of the convolution $W_{\omega_{\mathrm{CL}}}(\Delta t,E_1,E_2) = \int_{-\infty}^{\infty} dt_2\, W(\Delta t+t_2,t_2,E_1+\hbar\omega_{\mathrm{CL}}/2,E_2+\hbar\omega_{\mathrm{CL}}/2)$ [see bottom panel in Fig. 5(d)].